Artificial effectors with implications for biotechnology. We have shown that the repeat region of TAL effectors has a sequential nature that corresponds to a consecutive target DNA sequence. Hence, it should be feasible to generate effectors with novel DNA binding specificities. Seven artificial effectors (ArtX) were generated, three with 10.5 and four with 12.5 randomly assembled repeats. They were constructed as N-terminal fusions to GFP and tested for induction of *Bs4* promoter-reporter fusions containing predicted target DNA sequences. All seven effectors induced the GUS reporter only in the presence of the corresponding target DNA box (three are shown in Fig. 3, C to E, and fig. S8). The effectors showed GFP fluorescence exclusively in the plant cell nucleus after *Agrobacterium*-mediated expression, indicating the production of full-length proteins. This shows that we are able to design DNA binding domains that target a specific DNA sequence.

Our code for recognition specificity of TAL effectors solved a 20-year enigma dating from the cloning of *avrBs3*, the first TAL effector gene (*26*). The repeat region mediates direct binding to DNA (*9*). Here, we discover how target specificity is encoded. One repeat corresponds to one base pair in the DNA, and the tandem array of repeats corresponds to a consecutive DNA sequence. Target DNA specificity is based on a two–amino acid motif per repeat, enabling the deduction of a simple code to predict the DNA target preference of TAL effectors. We have experimentally identified the following recognition preferences: HD = C; NG = T; NI = A; NS = A, C, G, or T; NN = A or G; and IG = T. Because many TAL effectors are major virulence factors (*4*, *5*), the knowledge of host targets will enhance our understanding of plant disease development caused by xanthomonads.

In addition, we successfully designed artificial TAL effectors that act as transcription factors with novel DNA-binding specificities. Zinc finger transcription factors, which encode DNA binding specificity in their tandem zinc finger units, have been engineered to bind chosen DNA sequences, leading to gene control systems of great utility for biotechnology (*27*, *28*). Similarly, the TAL effectors use a DNA binding code that can be exploited to generate DNA binding domains for any DNA target.

References and Notes

1. T. Boller, S. Y. He, *Science* **324**, 742 (2009).
2. V. Göhre, S. Robatzek, *Annu. Rev. Phytopathol.* **46**, 189 (2008).
3. J. D. Jones, J. L. Dangl, *Nature* **444**, 323 (2006).
4. S. Kay, U. Bonas, *Curr. Opin. Microbiol.* **12**, 37 (2009).
5. F. F. White, B. Yang, *Plant Physiol.* **150**, 1677 (2009).
6. J. Bai, S.-H. Choi, G. Ponciano, H. Leung, J. E. Leach, *Mol. Plant Microbe Interact.* **13**, 1322 (2000).
7. B. Yang, F. F. White, *Mol. Plant Microbe Interact.* **17**, 1192 (2004).
8. K. Gu *et al.*, *Nature* **435**, 1122 (2005).
9. S. Kay, S. Hahn, E. Marois, G. Hause, U. Bonas, *Science* **318**, 648 (2007).
10. P. Römer *et al.*, *Science* **318**, 645 (2007).
11. S. Schornack, A. Meyer, P. Römer, T. Jordan, T. Lahaye, *J. Plant Physiol.* **163**, 256 (2006).
12. A. Sugio, B. Yang, T. Zhu, F. F. White, *Proc. Natl. Acad. Sci. U.S.A.* **104**, 10720 (2007).
13. B. Yang, A. Sugio, F. F. White, *Proc. Natl. Acad. Sci. U.S.A.* **103**, 10503 (2006).
14. S. Kay, S. Hahn, E. Marois, R. Wieduwild, U. Bonas, *Plant J.* **59**, 859 (2009).
15. G. Van den Ackerveken, E. Marois, U. Bonas, *Cell* **87**, 1307 (1996).
16. W. Zhu, B. Yang, J. M. Chittoor, L. B. Johnson, F. F. White, *Mol. Plant Microbe Interact.* **11**, 824 (1998).
17. K. Herbers, J. Conrads-Strauch, U. Bonas, *Nature* **356**, 172 (1992).
18. B. Yang, A. Sugio, F. F. White, *Mol. Plant Microbe Interact.* **18**, 142 (2005).
19. E. Marois, G. Van den Ackerveken, U. Bonas, *Mol. Plant Microbe Interact.* **15**, 637 (2002).
20. P. Römer *et al.*, *Plant Physiol.* **150**, 1697 (2009).
21. Single-letter abbreviations for the amino acid residues are as follows: A, Ala; C, Cys; D, Asp; E, Glu; F, Phe; G, Gly; H, His; I, Ile; K, Lys; L, Leu; M, Met; N, Asn; P, Pro; Q, Gln; R, Arg; S, Ser; T, Thr; V, Val; W, Trp; and Y, Tyr.
22. Materials and methods are available as supporting material on *Science* Online.
23. S. Kay, J. Boch, U. Bonas, *Mol. Plant Microbe Interact.* **18**, 838 (2005).
24. S. Schornack, K. Peter, U. Bonas, T. Lahaye, *Mol. Plant Microbe Interact.* **18**, 1215 (2005).
25. J. O. Borevitz, Y. Xia, J. Blount, R. A. Dixon, C. Lamb, *Plant Cell* **12**, 2383 (2000).
26. U. Bonas, R. E. Stall, B. J. Staskawicz, *Mol. Gen. Genet.* **218**, 127 (1989).
27. J. R. Desjarlais, J. M. Berg, *Proc. Natl. Acad. Sci. U.S.A.* **89**, 7345 (1992).
28. J. A. Townsend *et al.*, *Nature* **459**, 442 (2009).

29. We thank J. Streubel, A. Richter, and P. Römer for kindly providing constructs; T. Gonzalez for advice on anthocyanin synthesis; and R. Kahmann for helpful suggestions on the manuscript. A patent covering the findings is pending. This work was supported by grants from the Deutsche Forschungsgemeinschaft (SPP 1212 to J.B. and U.B. and SFB 648 to U.B.).

Supporting Online Material

www.sciencemag.org/cgi/content/full/1178811/DC1
Materials and Methods
Figs. S1 to S10
Table S1
References

8 July 2009; accepted 23 September 2009
Published online 29 October 2009;
10.1126/science.1178811
Include this information when citing this paper.

REPORTS

Modulated High-Energy Gamma-Ray Emission from the Microquasar Cygnus X-3

The Fermi LAT Collaboration*†

Microquasars are accreting black holes or neutron stars in binary systems with associated relativistic jets. Despite their frequent outburst activity, they have never been unambiguously detected emitting high-energy gamma rays. The Fermi Large Area Telescope (LAT) has detected a variable high-energy source coinciding with the position of the x-ray binary and microquasar Cygnus X-3. Its identification with Cygnus X-3 is secured by the detection of its orbital period in gamma rays, as well as the correlation of the LAT flux with radio emission from the relativistic jets of Cygnus X-3. The gamma-ray emission probably originates from within the binary system, opening new areas in which to study the formation of relativistic jets.

Cygnus X-3 (Cyg X-3) motivated to a large extent the development of high-energy gamma-ray astronomy. Detections of Cyg X-3 were reported in the 1970s and early 1980s at energies of tens of mega–electron volts, tera–electron volts, peta–electron volts, and possibly exa–electron volts, generating considerable excitement as these identified the system as a prime source of cosmic rays (*1*–*3*). However, the detections remained doubtful in part because observations in the late 1980s and in the 1990s by a more sensitive generation of ground-based telescopes failed to confirm the tera–electron volt and peta–electron volt detection of Cyg X-3 (*4*, *5*), and also because both the COS-B satellite (*6*) and the CGRO-EGRET satellite (*7*) could not find emission from the source in the giga–electron volt range.

Here, we report the detection of a variable high-energy gamma-ray (100 MeV to 100 GeV) source that we identify with Cyg X-3 based on its location, the detection of a modulation of the gamma-ray flux at the orbital period of the binary system, and the gamma-ray variability correlated with the radio emission originating from the relativistic jets of Cyg X-3.

Cyg X-3 is a high-mass x-ray binary system (*2*) with a short orbital period of 4.8 hours (*8*), located in the Galactic plane at a distance of ~7 kpc from Earth (*9*). The nature of the compact object—neutron star or black hole—is still subject

to debate; however, the companion is known to be the Wolf-Rayet star V1521 Cyg (*10*). After its discovery in 1966 (*11*), Cyg X-3 was intensively observed over a wide range of wavelengths. It frequently becomes the brightest radio source among the binary systems with major flares because of its relativistic jets (*12*–*14*), which qualify the source as a microquasar. The variable emission observed from microquasars, ranging from radio frequencies up to a few hundreds of kilo–electron volts, is induced by the interplay between the stellar companion, the accretion flow, the optically thin electron corona, and the relativistic jets (*15*–*17*).

We present the results of the Fermi Large Area Telescope (LAT) observations of the Cygnus region between 4 August 2008 and 2 September 2009 [see the supporting online material (SOM) for details] (Fig. 1). The pulsar PSR J2032+4127 is located very close (~30 arc min) to Cyg X-3 and contributes substantially to the LAT photons at the location of Cyg X-3. However, because it exhibits relatively narrow pulses (*18*), it enabled us to select the LAT data using the off-pulse phase intervals of PSR J2032+4127, a procedure that preserves 80% of LAT live time. We then performed an unbinned maximum-likelihood spectral and spatial fitting analysis of a 15°-radius region centered on the position of Cyg X-3. Adding a source consistent with the location of Cyg X-3 in the fitting procedure improves the fit significantly. The overall significance of the LAT source at this position amounts to more than 29 standard deviations (29σ). The position of the LAT source is right ascension (J2000) = 308.05° and declination (J2000) = 40.96° with a statistical uncertainty (95% confidence level) of 0.04°, which is consistent with the location of Cyg X-3.

We also constructed the LAT light curve on 4-day (Fig. 2) and 2-day time scales in order to highlight the gamma-ray variability of the LAT source, which is mostly dominated by two main active periods: 11 October to 20 December 2008 [modified Julian date (MJD) 54750 to 54820] and 8 June to 2 August 2009 (MJD 54990 to 55045). These phases of activity may be consistent with one or several flares, with the brightest flare possibly being observed at the end of each period. The peak flux can be as high as ~2×10^{-6} photons cm^{-2} s^{-1} above 100 MeV.

We have fitted the spectrum of Cyg X-3 in the two active periods with a simple power law using the data set created from the off-pulse phase intervals of PSR J2032+4127. We obtained a spectral index Γ of 2.70 ± 0.05 [statistical (stat)] ± 0.20 [systematic (syst)]. The systematic error was estimated by using different sets of models for the diffuse emission. In view of the soft spectrum and the bright, complex, diffuse emission in this region, this spectral parameter may have a larger systematic uncertainty. However, for this preliminary spectral index, the average photon flux of the LAT source in the active periods is [1.19 ± 0.06 (stat) ± 0.37 (syst)] × 10^{-6} photons cm^{-2} s^{-1} above 100 MeV, corresponding to an energy flux of [4.0 ± 0.3 (stat) ± 1.3 (syst)] × 10^{-10} erg cm^{-2} s^{-1}. This corresponds to a gamma-ray luminosity L_γ of ~ 3×10^{36} (distance/7 kpc)^2 erg s^{-1}, which is similar to what was originally reported by the SAS-2 satellite (*19*) in the early 1970s for Cyg X-3 in a similar energy range. The AGILE satellite also reported gamma-ray flares in the vicinity of Cyg X-3 at a similar epoch (*20*).

To securely identify the LAT source with Cyg X-3, we performed a timing analysis to search for the 4.8-hour orbital period (*8*) of Cyg X-3. For that purpose, we created a light curve for the LAT source using aperture photometry and 1000-s time bins. We extracted photons within a circular region with a radius of 1°, centered on Cyg X-3 in the energy range from 100 MeV to 100 GeV. We calculated the power spectra for both the entire light curve and also for only the active periods identified above (Fig. 2). Because 1000 s is shorter than the sky survey rocking period of Fermi, the exposure of Cyg X-3 varies considerably from time bin to time bin. We therefore weighted the contribution of data points to the power spectrum by their relative exposures. Although no orbital modulation is apparent when the entire data set is used, two peaks, corresponding to the orbital period of Cyg X-3 and its second harmonic (in addition to low-frequency noise), stand out when the analysis is restricted to the two periods of enhanced emission (Fig. 3A). The nominal probability of a false detection for a period of arbitrary frequency is 3.6 × 10^{-5}, taking into account the number of trials. To investigate whether the modulation seen at the orbital period of Cyg X-3 could be an artifact, we also extracted light curves and calculated power spectra for all sources in the Fermi Bright Source List. In no case did we see significant modulation at the orbital period of Cyg X-3. A maximum-likelihood analysis of light curve photons (SOM) shows that the probability of finding a modulation as strong as the LAT signal with the known period of Cyg X-3 is ~ 2.4 × 10^{-9}. This confirms that the LAT source displays the orbital period of Cyg X-3 and therefore secures its identification with Cyg X-3.

The orbital period of Cyg X-3 has been reported to show secular change (*21*). To obtain the predicted parameters of Cyg X-3 at the time of our LAT observations, we therefore used the parabolic ephemeris of Cyg X-3 (*21*) and derived a period of 0.199692441 (35) day and an epoch of minimum x-ray flux of MJD 54,856.693 (10). This is consistent with the period obtained—P = 0.199655 (46) day—from the maximum-likelihood analysis of the LAT light curve. We compared the LAT light curve from the active

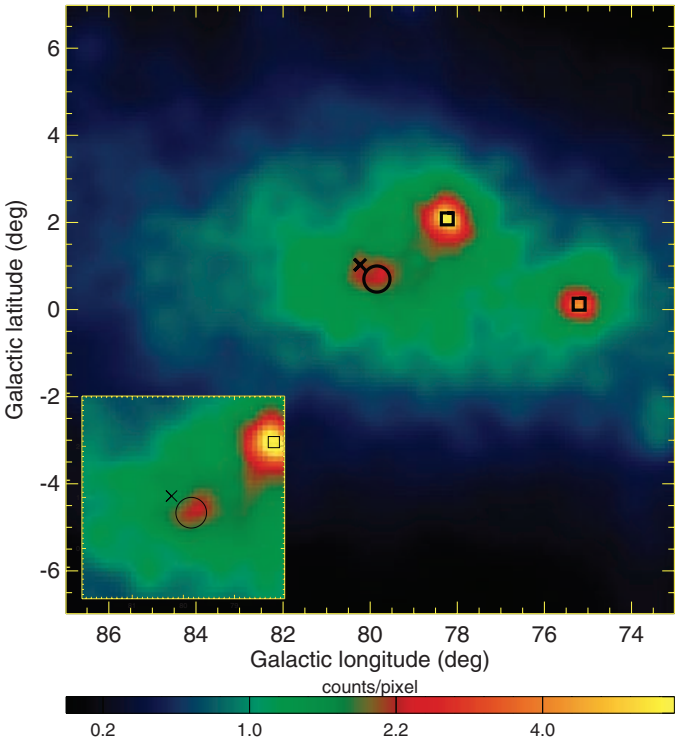

Fig. 1. 200-MeV to 100-GeV Fermi/LAT gamma-ray counts map of a 14° × 14° region centered on the position of Cyg X-3 and corresponding to the active periods discussed in the text. The map (with no background subtraction) was adaptively smoothed by imposing a minimum signal-to-noise ratio of 15. It shows the region around Cyg X-3 encompassing emission from three bright gamma-ray pulsars (PSR J2021+4026, PSR J2021+3651, and PSR J2032+4127), as well as the strong Galactic diffuse emission of the Cygnus region. The locations of PSR J2021+4026 and PSR J2021+3651 are indicated by black squares, and PSR J2032+4127 is indicated by a cross. The position of Cyg X-3 is shown by the circle. (Inset) Similar image for the central portion (4° × 4°), corresponding to the off-pulse data set from PSR J2032+4127 (which is not detected in the off-pulse data). A total of ~3400 counts were detected from the LAT gamma-ray source at the position of Cyg X-3.

*All authors with their affiliations appear at the end of this paper.
†To whom correspondence should be addressed. E-mail: stephane.corbel@cea.fr (S.C.); Robin.Corbet@nasa.gov (R.C.); Guillaume.Dubus@obs.ujf-grenoble.fr (G.D.)

time ranges folded on the orbital period to the folded 1.5- to 12-keV x-ray light curve of Cyg X-3 from the Rossi X-ray Timing Explore All-Sky Monitor (RXTE/ASM) (Fig. 3B). The folded x-ray and gamma-ray light curves have the same asymmetric shape, with a slow rise followed by a faster decay. However, a striking contrast is that the phase of LAT maximum flux is close to the phase of minimum x-ray count rate. Indeed, the LAT minimum trails the x-ray minimum by 0.3 to 0.4 in phase. Further observations will be needed to interpret the small (~0.1) shift in LAT maximum that occurs from the first to the second active period (SOM).

The soft x-ray light curves (1.5 to 12 keV) from the RXTE/ASM and hard x-ray light curves (15 to 50 keV) from the Swift/BAT satellite indicate that all LAT gamma-ray active periods from Cyg X-3 correspond to the soft x-ray state of the source (fig. S2). Cyg X-3 is known to flare in radio in the soft state (*22*), with associated relativistic plasma ejection events (*12*–*14*). We have therefore compiled the radio data from our regular monitoring with the AMI telescope and the OVRO 40-m telescope at 15 GHz. Inspection of the LAT and radio light curves of Cyg X-3 (Fig. 2) indicates that the LAT active periods occur close to radio flares. To quantify the relation between the gamma-ray and radio emission, we have calculated the discrete cross-correlation function normalized only by the sample variance (fig. S3). We find a positive correlation between the two wave bands. The overall correlation is dominated by the strong radio and gamma-ray flare around MJD 54810. The peak in the cross-correlation is significant at more than ~3σ (the exact value depending on the assumed noise properties of the LAT data on Cyg X-3). The lag of the radio light curve to the gamma rays is not well constrained; a bootstrapping technique shows that it is 5 ±7 days.

The detection of Cyg X-3 by the LAT during periods of relativistic ejection events is important for linking and understanding the different components of an accreting binary system (the wind of the Wolf-Rayet star, the compact object, and the accretion disk, corona, and relativistic jets). A variable hard tail above 30 keV with a power law index $\Gamma \approx 2$ is present in some instances (the ultrasoft state) of the soft x-ray state associated with the onset of radio flaring episodes (*22*). The tail has been reported to extend up to several hundred kilo–electron volts (*23*). The Fermi flux is compatible with the extrapolation of this tail to 100 MeV but has a steeper spectrum, suggesting that we are seeing the high-energy end of a spectral component peaking in soft gamma rays.

The hard x-ray tail is typically modeled as being due to the Compton upscattering of photons from a soft photon source by high-energy electrons in a corona (possibly the base of the jets), although the physical processes responsible for the electrons' acceleration are not yet known (*22*, *23*). It is likely that the gamma-ray emission is due to the same process; however, this is only possible if the emission region is not too close to the accretion disk, or it would be absorbed by pair production on the soft x-ray photons (*24*). On the other hand, the gamma-ray modulation suggests (*25*) that the emission region size and location are bounded by the orbital separation $a \approx 2.5 \times 10^{11}$ cm.

With the emitting region located away from the accretion disk but within the system, the companion star provides the dominant radiation field at the location of the electrons. Electrons with energies of a few giga–electron volts can then inverse Compton-scatter the ultraviolet (UV) photons from the star [surface temperature (T_*) $\approx 10^5$ K] to gamma rays. The stellar radiation field is not isotropic for the electrons, so the upscattered emission also will be anisotropic, causing a modulation of the gamma-ray emission. Assuming that the location of the electrons is in phase with the compact object (as expected for jets perpendicular to the orbital plane), maximum gamma-ray emission occurs when the electrons are seen behind the Wolf-Rayet star; that is, at superior conjunction when the energetic electrons directed toward Earth suffer head-on collision with the stellar UV photons (*26*). This corresponds to minimum x-ray emission if the x-ray modulation is due to Compton scattering in the companion's wind as is usually presumed (*27*). Infrared studies also support this phasing of the orbit (*28*). The phase shift of the gamma-ray minimum (fig. S1) from $\phi = 0$ might be associated with misalignment of the axis of the jets.

The inverse Compton energy-loss time scale $t_{ic} \approx 1 E_{GeV}^{-1}$ s is short compared to the escape time scale $t_{esc} = a/c \approx 8$ s, meaning that this radiative process is quite efficient. The maximum observed gamma-ray luminosity L_γ is $5 \times 10^{36} d_{7kpc}^2$ erg s^{-1} above 100 MeV (for a spectral index of $\Gamma = 2.7$), which is ≲10% of the x-ray luminosity, suggesting that only a minor fraction of the accretion power is released via particle acceleration. This contrasts with the few other binaries (*29*) that are confirmed as high-energy gamma-ray emitters. In these, the dominance of gamma rays in the nonstellar radiative output, the weakness of the x-ray emission

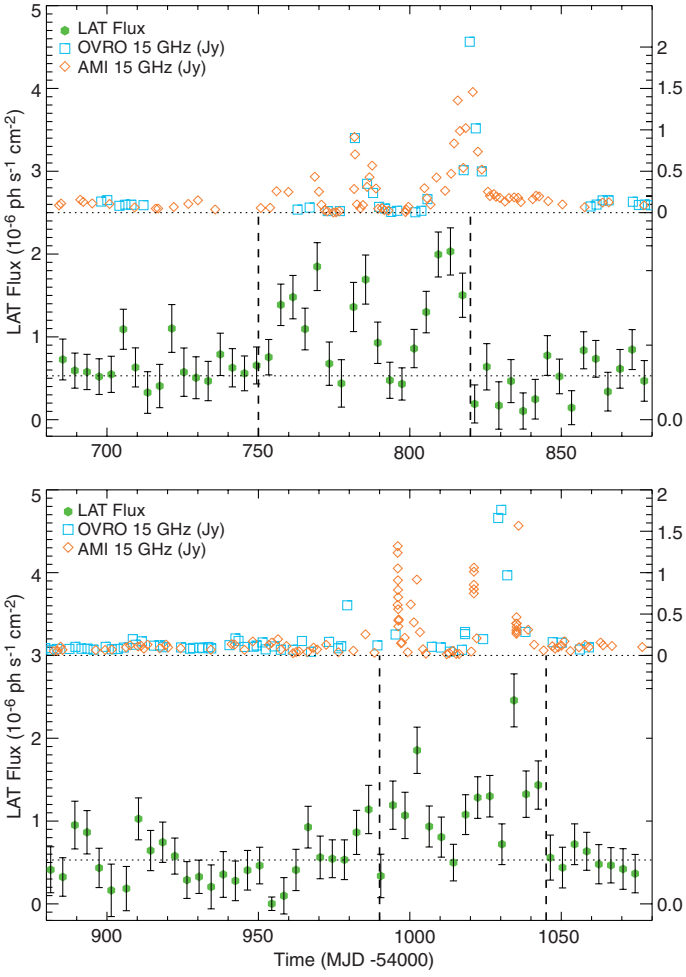

Fig. 2. Gamma-ray light curve in two parts (top and bottom panels) with a likelihood analysis window of 4 days of the LAT source at the location of Cyg X-3. The LAT fluxes (left axis) are expressed in units of 10^{-6} photons cm^{-2} s^{-1} above 100 MeV. A power law shape with spectral index of 2.7 is assumed for Cyg X-3 in the analysis. The parameters of the components for the model of the diffuse emission were held fixed to the values obtained in the global fit, with the exception of the normalization of the Galactic diffuse component that was left free. The vertical dashed lines illustrate the active periods discussed in the text. The bottom horizontal dotted line in each panel indicates the average gamma-ray flux at the location of Cyg X-3 outside the active periods. In addition, at the top of each panel, we show the Cyg X-3 15-GHz radio flux (from the AMI and OVRO 40-m radio telescopes) as a function of time (axis on the right). An offset of 0.124 Jy has been removed from the OVRO data to account for the effect of extended nearby sources that are resolved out by the AMI interferometer. A horizontal dotted line at 0 Jy is also plotted for reference. Several radio flares were detected during the LAT active periods.

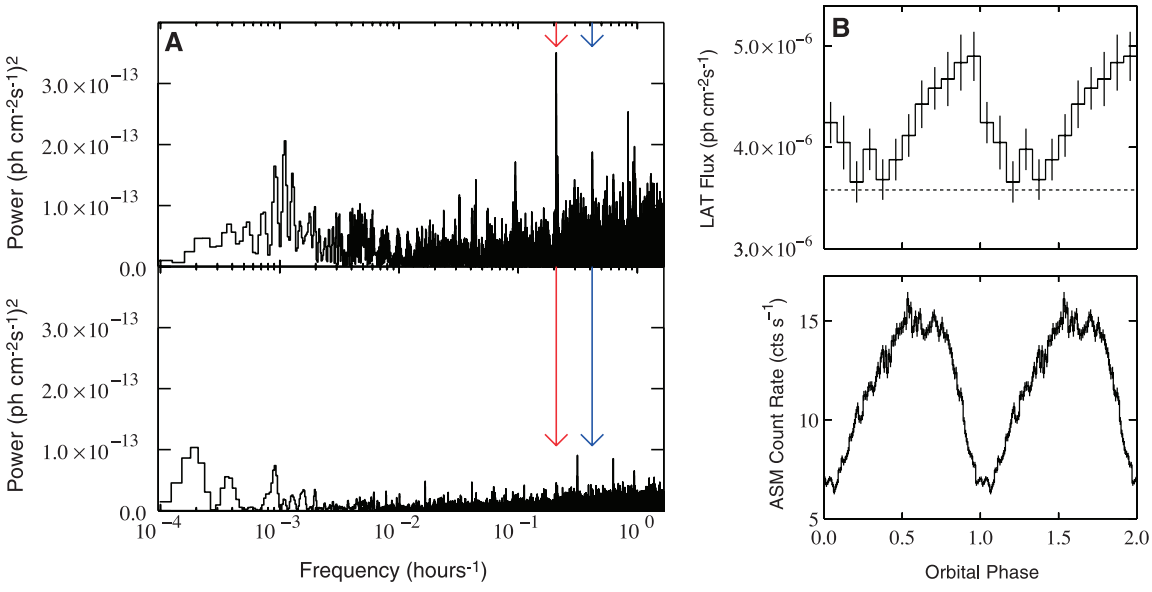

Fig. 3. Power spectra and folded light curves of the LAT source at the location of Cyg X-3. (**A**) (Bottom) Power spectrum of the entire LAT light curve. (Top) Power spectrum of the identified active periods of the LAT source. The red and blue arrows indicate the frequencies that correspond to the orbital period and the second harmonic of the orbital period, respectively. (**B**) (Top) Light curve of Cyg X-3 during times identified as the active intervals [same as top panel in (A)] of the LAT source folded on the orbital period of the system. The data points were again weighted by their exposures. The dashed line shows the emission level (including diffuse emission) obtained by measuring the flux in the 1° aperture outside the active periods of Cyg X-3. In our definition, the compact object is directly behind the star at phase = 0 (superior conjunction). (Bottom) RXTE ASM light curve of Cyg X-3 folded on the orbital period. The light curve is built with the data over the entire lifetime of RXTE.

($<10^{34}$ erg s^{-1}), and the lack of accretion signatures suggest a compact pulsar wind (*30*).

Interpreted as the propagation time of relativistic ejecta, the 5-day delay (still uncertain, however) between the onset of gamma-ray and radio flaring implies that the radio emission occurs at $\approx 1.3 \times 10^{16}$ cm [≈900 astronomical units ≈ 125 milli–arc sec (mas)] away from the system. Indeed, radio emission during flares is known to occur farther out in the jet on scales of hundreds of astronomical units (at a distance from the core of few tens of milli–arc seconds), with measured projected expansion velocities around 10 mas/day [0.5 to 0.6 *c* (*14*)].

Unique characteristics of Cyg X-3 as compared to all other microquasars are the very tight orbit and very strong Wolf-Rayet wind. With a wind mass loss $\sim 10^{-5}$ solar mass $year^{-1}$ and a wind velocity ~1000 km s^{-1} (*10*), the densities (hereafter n_{13} in units of 10^{13} cm^{-3}) reach 10^{13} cm^{-3} at the location of the compact object, which is orders of magnitude more than in all other systems. Thus, although we have discussed a leptonic origin for the giga–electron volt photons, if cosmic ray protons are also accelerated in the source, they could have substantial interaction with the nuclei in the stellar wind, producing charged and neutral pions that would decay into gamma rays and neutrinos. The time scale for proton-proton interaction is $t_{pp} \approx 100 n_{13}^{-1}\,\mathrm{s} > t_{esc}$. Assuming a 10% transfer efficiency of the proton energy into secondary particles, the required proton luminosity is $\sim 10(t_{pp}/t_{esc})L_\gamma$. Thus, the nonthermal energy would be larger than or (if the protons are confined) comparable to the x-ray luminosity. If this scenario is correct, something that the observation of neutrinos from this source would confirm, then the dense environment of Cyg X-3 could provide an opportunity to study the high-energy proton content in microquasars and their contribution to cosmic ray protons.

References and Notes

1. T. C. Weekes, *Phys. Rep.* **160**, 1 (1988).
2. J. M. Bonnet-Bidaud, G. Chardin, *Phys. Rep.* **170**, 325 (1988).
3. R. A. Ong, *Phys. Rep.* **305**, 93 (1998).
4. K. S. O'Flaherty *et al.*, *Astrophys. J.* **396**, 674 (1992).
5. A. Borione *et al.*, *Phys. Rev. D Part. Fields* **55**, 1714 (1997).
6. W. Hermsen *et al.*, *Astron. Astrophys.* **175**, 141 (1987).
7. M. Mori *et al.*, *Astrophys. J.* **476**, 842 (1997).
8. D. R. Parsignault *et al.*, *Nature* **239**, 123 (1972).
9. Z. Ling, S. N. Zhang, S. Tang, *Astrophys. J.* **695**, 1111 (2009).
10. M. H. van Kerkwijk, T. R. Geballe, D. L. King, M. van der Klis, J. van Paradijs, *Astron. Astrophys.* **314**, 521 (1996).
11. R. Giacconi, P. Go`renstein, H. Gursky, J. R. Waters, *Astrophys. J.* **148**, L119 (1967).
12. A. J. Mioduszewski, M. P. Rupen, R. M. Hjellming, G. G. Pooley, E. B. Waltman, *Astrophys. J.* **553**, 766 (2001).
13. J. C. A. Miller-Jones *et al.*, *Astrophys. J.* **600**, 368 (2004).
14. V. Tudose *et al.*, *Mon. Not. R. Astron. Soc.* **375**, L11 (2007).
15. I. F. Mirabel, L. F. Rodríguez, *Annu. Rev. Astron. Astrophys.* **37**, 409 (1999).
16. R. Fender, *Compact Stellar X-ray Sources*, Cambridge Astrophysics Series, no. 39, W. H. G. Lewin, M. van der Klis, Eds. (Cambridge Univ. Press, Cambridge, 2006).
17. R. A. Remillard, J. E. McClintock, *Annu. Rev. Astron. Astrophys.* **44**, 49 (2006).
18. F. Camilo *et al.*, *Astrophys. J.* **705**, 1 (2009).
19. R. C. Lamb, C. E. Fichtel, R. C. Hartman, D. A. Kniffen, D. J. Thompson, *Astrophys. J.* **212**, L63 (1977).
20. M. Tavani *et al.*, http://lanl.arxiv.org/abs/0910.5344.
21. N. S. Singh *et al.*, *Astron. Astrophys.* **392**, 161 (2002).
22. A. Szostek, A. A. Zdziarski, M. L. McCollough, *Mon. Not. R. Astron. Soc.* **388**, 1001 (2008).
23. L. Hjalmarsdotter, A. A. Zdziarski, A. Szostek, D. C. Hannikainen, *Mon. Not. R. Astron. Soc.* **392**, 251 (2009).
24. A. Carramiñana, *Astron. Astrophys.* **264**, 127 (1992).
25. The orbital modulation on its own does not limit the size of the emitting region to the size of the binary orbit, because the orbital period could be imprinted on the emission occurring further out. However, the interpretation of the modulation as inverse Compton scattering off stellar photons requires the high-energy electrons to be within the system.
26. The gamma rays in the Fermi energy range are unaffected by Compton scattering in the stellar wind or by pair production on the stellar UV photons.
27. J. Pringle, *Nature* **247**, 21 (1974).
28. M. M. Hanson, M. D. Still, R. P. Fender, *Astrophys. J.* **541**, 308 (2000).
29. A. A. Abdo *et al.*, *Astrophys. J.* **701**, L123 (2009).
30. G. Dubus, *Astron. Astrophys.* **456**, 801 (2006).

31. The Fermi LAT Collaboration acknowledges support from a number of agencies and institutes for both development and the operation of the LAT as well as scientific data analysis. These include NASA and the Department of Energy in the United States; CEA/Institut de Recherches sur les lois Fondamentales de l'Univers and l'Institut National de Physique Nucléaire et de Physique des Particules/CNRS in France; the Agenzia Spaziale Italiana and Istituto Nazionale di Fisica Nucleare in Italy; the Ministry of Education, Culture, Sports, Science and Technology, National Laboratory for High Energy Physics (KEK), and Japan Aerospace Exploration Agency in Japan; and the K. A. Wallenberg Foundation, Swedish Research Council and National Space Board in Sweden. Additional support from the Istituto Nazionale di Astrofisica in Italy and the Centre National d'Etudes Spatiales in France for science analysis during the operations phase is also gratefully acknowledged. J.C. is a Royal Swedish Academy of Sciences Research Fellow, funded by a grant from the K. A. Wallenberg Foundation. G.D. and A.B.H. are funded by contract ERC-StG-200911 from the European Community.

The Fermi LAT Collaboration

A. A. Abdo,[1,2] M. Ackermann,[3] M. Ajello,[3] M. Axelsson,[4,5] L. Baldini,[6] J. Ballet,[7] G. Barbiellini,[8,9] D. Bastieri,[10,11] B. M. Baughman,[12] K. Bechtol,[3] R. Bellazzini,[6] B. Berenji,[3] R. D. Blandford,[3] E. D. Bloom,[3] E. Bonamente,[13,14] A. W. Borgland,[3] A. Brez,[6] M. Brigida,[15,16] P. Bruel,[17] T. H. Burnett,[18] S. Buson,[11] G. A. Caliandro,[19] R. A. Cameron,[3] P. A. Caraveo,[20] J. M. Casandjian,[7] C. Cecchi,[13,14] Ö. Çelik,[21,22,23] S. Chaty,[7] C. C. Cheung,[1,2] J. Chiang,[3] S. Ciprini,[14] R. Claus,[3] J. Cohen-Tanugi,[24] L. R. Cominsky,[25] J. Conrad,[26,5] S. Corbel,[7,27]* R. Corbet,[21,23]* C. D. Dermer,[1] F. de Palma,[15,16] S.W. Digel,[3] E. do Couto e Silva,[3] P. S. Drell,[3] R. Dubois,[3] G. Dubus,[28]* D. Dumora,[29,30] C. Farnier,[24] C. Favuzzi,[15,16] S. J. Fegan,[17] W. B. Focke,[3] P. Fortin,[17] M. Frailis,[31] P. Fusco,[15,16] F. Gargano,[16] N. Gehrels,[21,32,33] S. Germani,[13,14] G. Giavitto,[8,9] B. Giebels,[17] N. Giglietto,[15,16] F. Giordano,[15,16] T. Glanzman,[3] G. Godfrey,[3] I. A. Grenier,[7] M.-H. Grondin,[29,30] J. E. Grove,[1] L. Guillemot,[34]

S. Guiriec,[35] Y. Hanabata,[36] A.K. Harding,[21] M. Hayashida,[3] E. Hays,[21] A. B. Hill,[28] L. Hjalmarsdotter,[4,5] D. Horan,[17] R. E. Hughes,[12] M. S. Jackson,[5,37] G. Jóhannesson,[3] A. S. Johnson,[3] T. J. Johnson,[21,33] W. N. Johnson,[1] T. Kamae,[3] H. Katagiri,[36] N. Kawai,[38,39] M. Kerr,[18] J. Knödlseder,[42] M. L. Kocian,[3] E. Koerding,[7] M. Kuss,[6] J. Lande,[3] L. Latronico,[6] M. Lemoine-Goumard,[29,30] F. Longo,[8,9] F. Loparco,[15,16] B. Lott,[29,30] M. N. Lovellette,[1] P. Lubrano,[13,14] G. M. Madejski,[3] A. Makeev,[1,41] L. Marchand,[42] M. Marelli,[20] W. Max-Moerbeck,[43] M. N. Mazziotta,[16] N. McColl,[42] J. E. McEnery,[21,33] C. Meurer,[26,5] P. F. Michelson,[3] S. Migliari,[44] W. Mitthumsiri,[3] T. Mizuno,[36] C. Monte,[15,16] M. E. Monzani,[3] A. Morselli,[45] I. V. Moskalenko,[3] S. Murgia,[3] P. L. Nolan,[3] J. P. Norris,[46] E. Nuss,[24] T. Ohsugi,[36] N. Omodei,[6] R. A. Ong,[42] J. F. Ormes,[46] D. Paneque,[3] D. Parent,[29,30] V. Pelassa,[24] M. Pepe,[13,14] M. Pesce-Rollins,[6] F. Piron,[24] G. Pooley,[47] T. A. Porter,[48] K. Pottschmidt,[21] S. Rainò,[15,16] R. Rando,[10,11] P. S. Ray,[1] M. Razzano,[6] N. Rea,[19,49] A. Readhead,[43] A. Reimer,[50,3] O. Reimer,[50,3] J. L. Richards,[43] L. S. Rochester,[3] J. Rodriguez,[7] A. Y. Rodriguez,[19] R. W. Romani,[3] F. Ryde,[37,5] H. F.-W. Sadrozinski,[48] A. Sander,[12] P. M. Saz Parkinson,[48] C. Sgrò,[6] E. J. Siskind,[51] D. A. Smith,[29,30] P. D. Smith,[12] P. Spinelli,[15,16] J.-L. Starck,[7] M. Stevenson,[43] M. S. Strickman,[1] D. J. Suson,[52] H. Takahashi,[36,11] T. Tanaka,[3] J. B. Thayer,[3] D. J. Thompson,[21] L. Tibaldo,[10,11,7] J. A. Tomsick,[53] D. F. Torres,[54,19] G. Tosti,[13,14] A. Tramacere,[3,55] Y. Uchiyama,[3] T. L. Usher,[3] V. Vasileiou,[22,23] N. Vilchez,[40] V. Vitale,[45,56] A. P. Waite,[3] P. Wang,[3] J. Wilms,[57] B. L. Winer,[12] K. S. Wood,[1] T. Ylinen,[37,58,5] M. Ziegler[48]

[1]Space Science Division, Naval Research Laboratory, Washington, DC 20375, USA. [2]National Research Council Research Associate, National Academy of Sciences, Washington, DC 20001, USA. [3]W. W. Hansen Experimental Physics Laboratory, Kavli Institute for Particle Astrophysics and Cosmology, Department of Physics and SLAC National Accelerator Laboratory, Stanford University, Stanford, CA 94305, USA. [4]Department of Astronomy, Stockholm University, SE-106 91 Stockholm, Sweden. [5]The Oskar Klein Centre for Cosmoparticle Physics, AlbaNova, SE-106 91 Stockholm, Sweden. [6]Istituto Nazionale di Fisica Nucleare, Sezione di Pisa, I-56127 Pisa, Italy. [7]Laboratoire AIM, CEA-IRFU/CNRS/Université Paris Diderot, Service d'Astrophysique, CEA Saclay, 91191 Gif sur Yvette, France. [8]Istituto Nazionale di Fisica Nucleare, Sezione di Trieste, I-34127 Trieste, Italy. [9]Dipartimento di Fisica, Università di Trieste, I-34127 Trieste, Italy. [10]Istituto Nazionale di Fisica Nucleare, Sezione di Padova, I-35131 Padova, Italy. [11]Dipartimento di Fisica "G. Galilei," Università di Padova, I-35131 Padova, Italy. [12]Department of Physics, Center for Cosmology and Astro-Particle Physics, Ohio State University, Columbus, OH 43210, USA. [13]Istituto Nazionale di Fisica Nucleare, Sezione di Perugia, I-06123 Perugia, Italy. [14]Dipartimento di Fisica, Università degli Studi di Perugia, I-06123 Perugia, Italy. [15]Dipartimento di Fisica "M. Merlin" dell'Università e del Politecnico di Bari, I-70126 Bari, Italy. [16]Istituto Nazionale di Fisica Nucleare, Sezione di Bari, 70126 Bari, Italy. [17]Laboratoire Leprince-Ringuet, École polytechnique, CNRS/IN2P3, Palaiseau, France. [18]Department of Physics, University of Washington, Seattle, WA 98195-1560, USA. [19]Institut de Ciencies de l'Espai (IEEC-CSIC), Campus UAB, 08193 Barcelona, Spain. [20]INAF-Istituto di Astrofisica Spaziale e Fisica Cosmica, I-20133 Milano, Italy. [21]NASA Goddard Space Flight Center, Greenbelt, MD 20771, USA. [22]Center for Research and Exploration in Space Science and Technology (CRESST) and NASA Goddard Space Flight Center, Greenbelt, MD 20771, USA. [23]Department of Physics and Center for Space Sciences and Technology, University of Maryland Baltimore County, Baltimore, MD 21250, USA. [24]Laboratoire de Physique Théorique et Astroparticules, Université Montpellier 2, CNRS/IN2P3, Montpellier, France. [25]Department of Physics and Astronomy, Sonoma State University, Rohnert Park, CA 94928-3609, USA. [26]Department of Physics, Stockholm University, AlbaNova, SE-106 91 Stockholm, Sweden. [27]Institut Universitaire de France, 75005 Paris, France. [28]Université Joseph Fourier-Grenoble 1/CNRS, Laboratoire d'Astrophysique de Grenoble (LAOG) UMR 5571, BP 53, 38041 Grenoble Cedex 09, France. [29]Université de Bordeaux, Centre d'Études Nucléaires Bordeaux Gradignan, UMR 5797, Gradignan, 33175, France. [30]CNRS/IN2P3, Centre d'Études Nucléaires Bordeaux Gradignan, UMR 5797, Gradignan, 33175, France. [31]Dipartimento di Fisica, Università di Udine and Istituto Nazionale di Fisica Nucleare, Sezione di Trieste, Gruppo Collegato di Udine, I-33100 Udine, Italy. [32]Department of Astronomy and Astrophysics, Pennsylvania State University, University Park, PA 16802, USA. [33]Department of Physics and Department of Astronomy, University of Maryland, College Park, MD 20742, USA. [34]Max-Planck-Institut für Radioastronomie, Auf dem Hügel 69, 53121 Bonn, Germany. [35]Center for Space Plasma and Aeronomic Research (CSPAR), University of Alabama in Huntsville, Huntsville, AL 35899, USA. [36]Department of Physical Sciences, Hiroshima University, Higashi-Hiroshima, Hiroshima 739-8526, Japan. [37]Department of Physics, Royal Institute of Technology (KTH), AlbaNova, SE-106 91 Stockholm, Sweden. [38]Department of Physics, Tokyo Institute of Technology, Meguro City, Tokyo 152-8551, Japan. [39]Cosmic Radiation Laboratory, Institute of Physical and Chemical Research (RIKEN), Wako, Saitama 351-0198, Japan. [40]Centre d'Étude Spatiale des Rayonnements, CNRS/UPS, BP 44346, F-30128 Toulouse Cedex 4, France. [41]George Mason University, Fairfax, VA 22030, USA. [42]Department of Physics and Astronomy, University of California, Los Angeles, CA 90095-1547, USA. [43]Cahill Center for Astronomy and Astrophysics, California Institute of Technology, Pasadena, CA 91125, USA. [44]European Space Astronomy Centre (ESAC), 28691 Villanueva de la Cañada, Madrid, Spain. [45]Istituto Nazionale di Fisica Nucleare, Sezione di Roma "Tor Vergata", I-00133 Roma, Italy. [46]Department of Physics and Astronomy, University of Denver, Denver, CO 80208, USA. [47]Cavendish Laboratory, Cambridge CB3 0HE, UK. [48]Santa Cruz Institute for Particle Physics, Department of Physics and Department of Astronomy and Astrophysics, University of California at Santa Cruz, Santa Cruz, CA 95064, USA. [49]Sterrenkundig Institut "Anton Pannekoek," 1098 SJ Amsterdam, Netherlands. [50]Institut für Astro- und Teilchenphysik and Institut für Theoretische Physik, Leopold-Franzens-Universität Innsbruck, A-6020 Innsbruck, Austria. [51]NYCB Real-Time Computing Inc., Lattingtown, NY 11560-1025, USA. [52]Department of Chemistry and Physics, Purdue University Calumet, Hammond, IN 46323-2094, USA. [53]Space Sciences Laboratory, University of California, Berkeley, CA 94720, USA. [54]Institució Catalana de Recerca i Estudis Avançats (ICREA), Barcelona, Spain. [55]Consorzio Interuniversitario per la Fisica Spaziale (CIFS), I-10133 Torino, Italy. [56]Dipartimento di Fisica, Università di Roma "Tor Vergata," I-00133 Roma, Italy. [57]Erlangen Centre for Astroparticle Physics, D-91058 Erlangen, Germany. [58]School of Pure and Applied Natural Sciences, University of Kalmar, SE-391 82 Kalmar, Sweden.

Supporting Online Material

www.sciencemag.org/cgi/content/full/1182174/DC1
Materials and Methods
Figs. S1 to S3
References

18 September 2009; accepted 5 November 2009
Published online 26 November 2009;
10.1126/science.1182174
Include this information when citing this paper.

Organic Nonvolatile Memory Transistors for Flexible Sensor Arrays

Tsuyoshi Sekitani,[1] Tomoyuki Yokota,[2] Ute Zschieschang,[3] Hagen Klauk,[3] Siegfried Bauer,[4] Ken Takeuchi,[1] Makoto Takamiya,[5] Takayasu Sakurai,[5] Takao Someya[1,2,6]*

Using organic transistors with a floating gate embedded in hybrid dielectrics that comprise a 2-nanometer-thick molecular self-assembled monolayer and a 4-nanometer-thick plasma-grown metal oxide, we have realized nonvolatile memory arrays on flexible plastic substrates. The small thickness of the dielectrics allows very small program and erase voltages (≤6 volts) to produce a large, nonvolatile, reversible threshold-voltage shift. The transistors endure more than 1000 program and erase cycles, which is within two orders of magnitude of silicon-based floating-gate transistors widely employed in flash memory. By integrating a flexible array of organic floating-gate transistors with a pressure-sensitive rubber sheet, we have realized a sensor matrix that detects the spatial distribution of applied mechanical pressure and stores the analog sensor input as a two-dimensional image over long periods of time.

Electronic devices are traditionally fabricated using inorganic semiconductors, rigid substrates, and high-temperature manufacturing methods. In contrast, organic semiconductors can be processed at low temperatures and on large-area polymeric substrates. This has allowed for the development of a variety of electronic devices on flexible plastic substrates, including solar cells (*1*), light-emitting diode displays (*2*), field-effect transistors (*3*), transponders (*4*), sensors (*5*), actuators (*6*), and nonvolatile memory transistors (*7*–*11*). Nonvolatile memory transistors are potentially useful to individualize radio-frequency transponders or to store data obtained by large-area sensor arrays for later read-out. Most of the organic memory transistors reported to date exploit the electric field–induced remnant polarization in ferroelectric polymer films (*7*–*11*). A considerable limitation of ferroelectric polymer memory transistors is that the coercive field required to reverse the macroscopic polarization increases with decreasing film thickness (*12*), which makes it difficult to obtain a large enough memory window with program and erase voltages below about 20 V. Also, due to the substantial surface roughness of the ferroelectric polymer films, the carrier field-effect mobility in these transistors is usually quite low (<0.1 cm^2/Vs).

[1]Department of Electrical and Electronic Engineering and Information Systems, The University of Tokyo, 7-3-1 Hongo, Bunkyo-ku, Tokyo 113-8656, Japan. [2]Department of Applied Physics, The University of Tokyo, 7-3-1 Hongo, Bunkyo-ku, Tokyo 113-8656, Japan. [3]Max Planck Institute for Solid State Research, Heisenbergstrasse 1, 70569 Stuttgart, Germany. [4]Soft Matter Physics (SOMAP), Johannes Kepler University Linz, A-4040 Linz, Austria. [5]Institute of Industrial Science, The University of Tokyo, 4-6-1 Komaba, Meguro-ku, Tokyo 153-8505 Japan. [6]Institute for Nano Quantum Information Electronics (INQIE), The University of Tokyo, 4-6-1 Komaba, Meguro-ku, Tokyo 153-8505 Japan.

*To whom correspondence should be addressed. E-mail: Someya@ee.t.u-tokyo.ac.jp.